QUARTERLY JOURNAL OF THE ROYAL METEOROLOGICAL SOCIETY

Q. J. R. Meteorol. Soc. **00**: 1–18 (2009)

Published online in Wiley InterScience

(www.interscience.wiley.com) DOI: 10.1002/qj.000

Can 4D-Var use Dynamical Information from Targeted Observations of a Baroclinic Structure?

E. A. Irvine[a]*, S. L. Gray[a], J. Methven[a]

[a]*University of Reading, UK*

Abstract: Targeted observations are generally taken in regions of high baroclinicity, but often show little impact. One plausible explanation is that important dynamical information, such as upshear tilt, is not extracted from the targeted observations by the data assimilation scheme and used to correct initial condition error. This is investigated by generating pseudo targeted observations which contain a singular vector (SV) structure that is not present in the background field or routine observations, i.e. assuming that the background has an initial condition error with tilted growing structure. Experiments were performed for a single case study with varying numbers of pseudo targeted observations. These were assimilated by the Met Office four-dimensional variational (4D-Var) data assimilation scheme, which uses a 6-hour window for observations and background error covariances calculated using the National Meteorological Centre (NMC) method. The forecasts were run using the operational Met Office Unified Model on a 24km grid. The results presented clearly demonstrate that a 6-hour window 4D-Var system is capable of extracting baroclinic information from a limited set of observations and using it to correct initial condition error. To capture the SV structure well, (projection of 0.72 in total energy) 50 sondes over an area of 1×10^6km^2 were required. When the SV was represented by only eight sondes along an example targeting flight track, covering a smaller area, the projection onto the SV structure was lower; the resulting forecast perturbations showed a SV structure with increased tilt and reduced initial energy. The total energy contained in the perturbations decreased as the SV structure was less well described by the set of observations (i.e. as fewer pseudo observations were assimilated). The assimilated perturbation had lower energy than the singular vector unless the pseudo observations were assimilated with the dropsonde observation errors halved from operational values.

KEY WORDS Singular vectors, background error covariance, variational data assimilation

Received December 2009

1 Introduction

During the past decade there have been many studies evaluating the potential benefit of using targeted observations as part of an adaptive observing network to improve forecasts of significant weather events. Dropsondes have generally been used to make the targeted observations. These are deployed from research aircraft into regions where the atmospheric state has been pre-determined to be sensitive to (small) perturbations to the initial conditions. The impact of these targeted observations on the downstream

*Correspondence to: Department of Meteorology, University of Reading, PO Box 243, Reading, Berkshire, RG6 6BB, UK. E-mail: e.a.irvine@reading.ac.uk

forecast has been somewhat mixed; large positive forecast impact was seen in the Fronts and Atlantic Storm Track Experiment (Montani *et al.*, 1999; Szunyogh *et al.*, 1999) and Winter Storm Reconnaissance Program (Szunyogh *et al.*, 2000, 2002), but much smaller positive impact was seen during the Atlantic THORPEX Regional Campaign (Fourrié *et al.*, 2006; Petersen and Thorpe, 2007) and Greenland Flow Distortion Experiment (GFDex; Irvine *et al.* (2009), hereafter referred to as IRV09). There are many reasons why targeted observations might fail to impact or even degrade the forecast. If the background error is too small so that the background is over-weighted compared to the observations, then the targeted observations will have little impact. IRV09 showed that for cases where the targeted observations were similar to the background field (i.e. contained little new information) that the magnitude of the forecast impact was small. The number of targeted observations and area that they cover is also an important factor (Leutbecher *et al.*, 2002); Buizza and Montani (1999) showed that under-sampling of the target region could result in a smaller forecast impact than theoretically possible from sampling the entire target region. Other studies (e.g. Langland (2005); Morss and Emanuel (2002)) have discussed limitations of the data assimilation scheme, and suggest that improvements to the formulation of data assimilation schemes may increase the impact of targeted observations. This paper explores the idea that the lack of impact could be due to the inability of the data assimilation scheme to make good use of the information contained within the targeted observations.

Targeted observations are often made in regions of high baroclinicity. This is evidenced in two ways. First, in making targeted observations we seek to reduce large forecast errors, usually those associated with the forecast of a severe weather event. These events are often associated with mid-latitude weather systems. As these systems are targeted 1-2 days before they make landfall, at the time of targeting they are still developing systems and therefore have a baroclinic structure. Second, SVs are one of the methods used to objectively determine where to make targeted observations, and have been used in various forms in most previous targeting experiments (see for example, Langland (2005)). Total energy singular vectors (TESVs) have been shown to identify the principal areas of cyclogenesis (regions of high baroclinicity) in the northern hemisphere. This is shown in Buizza and Palmer (1995) by comparison of the location of TESVs to regions of large values of the Eady Index (Hoskins and Valdes, 1990) which indicates the potential for baroclinic growth.

If the initial condition error has a baroclinic structure, this can lead to a large forecast error through rapid error growth. In order to reduce the magnitude of this type of error, the data assimilation scheme must be able to correct the initial condition error by producing a tilted analysis increment. This requires accurate specification of the background errors which control the spreading of observational data both in the horizontal and vertical. The initial background errors used in the Met Office 4D-Var scheme are climatological, calculated using the NMC method (Parrish and Derber, 1992), and are implicitly evolved during the assimilation window. The key elements in producing a tilted analysis increment are therefore the length of the assimilation window and the position of the observations within this window, as the longer the assimilation window the more appropriate the background errors become for the meteorological situation. Thépaut *et al.* (1996) used single observations at the end of assimilation windows of length 6-24 hours and found that to obtain an analysis increment with a baroclinic structure

DOI: 10.1002/qj

a 24-hour window was required. This contrasts with the results of Johnson *et al.* (2006), who found that 4D-Var was able to correct a growing initial error by using a time series of observations within only a 12-hour window. Unlike Thépaut *et al.* (1996) who used the full ECMWF 4D-Var scheme, Johnson *et al.* (2006) used a simplified 4D-Var scheme with a buoyancy control variable in the two-dimensional linear Eady model. This study extends the work of the previous studies by using the Met Office operational 4D-Var scheme (Rawlins *et al.*, 2007) with a 6-hour assimilation window, and the full nonlinear Met Office Unified Model (MetUM).

This study examines whether targeting may fail because the 4D-Var data assimilation scheme is unable to extract important dynamical information that is contained within the targeted observation and use it to correct initial condition error. This is tested by assimilating varying numbers of pseudo targeted observations, which contain a singular vector structure. This study uses one targeting case from the GFDex (Renfrew *et al.*, 2008), an aircraft-based field campaign that took place in Spring 2007 around Iceland and southern Greenland. IRV09 presented the results of the four targeting experiments from the GFDex and showed that the maximum impact of the targeted observations on the forecast for northern Europe was only 5% after 24 hours (in two of the four cases) and that for longer forecast times the forecasts were degraded by an equal amount. This paper is structured as follows. The choice of the GFDex targeting case study is motivated in Section 2.1. In Section 2.2 the structure and evolution of the singular vector used as the baroclinic structure in the pseudo targeted observations is presented. The generation of the pseudo targeted observations is discussed in Section 2.3 and the experimental setup in Section 2.4. The pseudo targeted observations are assimilated with a 4D-Var scheme; the structure of the resulting analysis increments is examined in Section 3 for different numbers of assimilated pseudo targeted observations. The evolution of the forecast perturbations by a nonlinear forecast model is examined in Section 4. The growth rate of the forecast perturbation is compared to that of the singular vector in Section 5 and conclusions are presented in Section 6.

2 Methodology

2.1 Targeting Case Study

This study uses the 01 March 2007 targeting case from the GFDex (presented in IRV09). The targeted dropsondes were released in the Irminger sea and Denmark Strait, in the region between Iceland and southern Greenland. This region had been identified by TESVs as a sensitive region for the 24 hour forecast over Scandinavia. The targeted sondes were released into an area of low pressure with high baroclinicity. At targeting time, a small cyclone was located in the lee of Greenland and there was weak barrier flow in the Denmark Strait. To the north-east of the target region, a polar low was forming, associated with an upper-level trough situated over the target region.

The impact of the targeted sondes moved with the developing polar low eastwards towards Scandinavia. IRV09 showed that the impact was due to the modification of the position of a tropopause fold that was associated with the development of the polar low. The 01 March case was chosen for this study because although the targeted observations caused some improvement to the forecast, the impact was small (maximum improvement and degradation of approximately 5%), despite the observations being different from the background. This is therefore a case where the data assimilation scheme did not appear to

DOI: 10.1002/qj

be able to make good use of the data from targeted observations taken in a baroclinic environment to correct the initial condition error.

2.2 The Baroclinic Structure

The leading ECMWF TESV from the 01 March 2007 targeting case is used as a proxy for a baroclinic structure that is contained within targeted observations, but missing from the background field. Therefore this TESV is also the structure of the assumed initial condition error. We thus consider an isolated initial condition error, that is well-sampled by targeted observations. This is different to operational targeting where a limited set of observations may capture only part of the initial condition error. The lead (forecast initialisation to targeting) and optimisation (targeting to forecast verification) times for the TESV used in this experiment were both 24 hours, with the growth optimised for a verification region over Scandinavia. This TESV was chosen because at targeting time at 1200 UTC on 01 March the initial TESV was located in the region of the flight track and after 24 hours the evolved TESV was located over Scandinavia, within the specified forecast verification region for the targeting experiments. The TESVs were provided by ECMWF during the GFDex field campaign, generated at T42 resolution using the ECMWF forecasting system.

Figure 1 shows the structure of the SV perturbations used in this experiment. Throughout this paper the perturbations will be displayed using the meridional wind component (v) and potential vorticity (PV) fields, from which the structure and growth of the SV can be clearly seen. The initial v and PV fields show a horizontally confined perturbation tilted against the direction of vertical wind shear (Figure 5(a) shows a profile of the zonal wind component (u)). This is consistent with Hartmann *et al.* (1995) who showed that at initial time singular vectors are confined to wave packets tilted against the vertical wind shear, with maximum amplitude in the mid-troposphere at short wavelengths. After 24 hours evolution the perturbations have untilted to some extent, have maximum amplitude near the tropopause and are located downstream of the original perturbations. Note that Figure 1 shows the SV perturbations multiplied by a factor of fifty. This was done to ensure that the observation minus background differences would be sufficient to result in some adjustment of the background towards the observations. The factor of fifty is motivated in the following section.

The TESV used is a dry TESV; this means that moisture was not taken into account in its calculation. The inclusion of moist processes such as latent heat release in the computation of TESVs has been shown to affect the location of the SV; although both dry and moist SVs are located in baroclinic regions, moist SVs are also located in frontal regions causing an enhancement or reduction in precipitation (Coutinho *et al.*, 2004). They also found that both dry and moist SVs have a similar structure and both types grow by PV unshielding, though the inclusion of moist processes results in smaller-scale SVs which exhibit enhanced growth rates.

The TESV structure for this case was available only at the initial and optimisation times. Also, as the SV calculation involves perturbation to a time-evolving control forecast in a primitive equation model, it is hard to interpret directly. To examine the evolution of the initial PV and the growth mechanisms responsible for producing the structure of the evolved TESV in Figure 1, the simpler framework of the Rossby wave model of De Vries *et al.* (2009) was used. This model solves the linearised quasi-geostrophic PV advection equation for an initial PV perturbation using a Green's function technique to associate velocities with PV anomalies at each level. The

DOI: 10.1002/qj

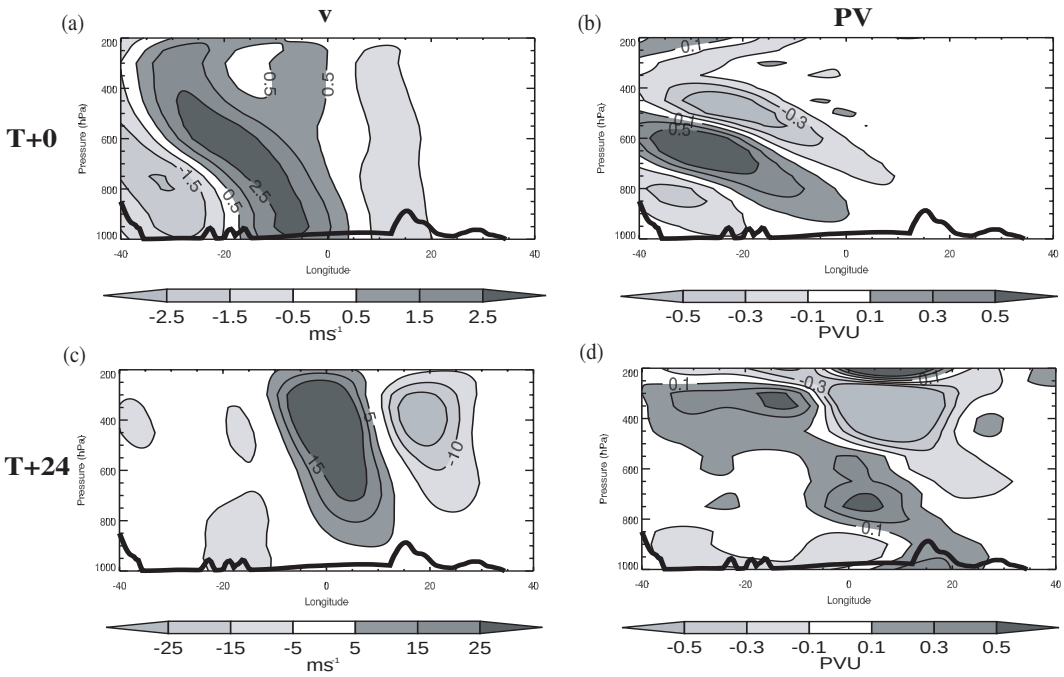

Figure 1. Cross-sections at 66°N from 40°W to 40°E through the initial (top) and evolved (bottom) singular vector for (a) and (c) meridional wind and (b) and (d) PV. The perturbations have been multiplied by a factor of fifty before plotting. The surface pressure (thick black line) is used to show the orography.

simple model considers perturbations to a steady, zonal flow and allows the evolution of the perturbations to be described almost completely in terms of three components: a tropospheric PV wave that tilts over in the shear and upper and lower counter-propagating Rossby wave (CRW) structures (which are each untilted but move relative to one another). The model was run on a beta-plane with idealised basic state conditions comparable to the atmospheric conditions in the 1200 UTC analysis: a linear wind profile with u=0ms^{-1} at the ground and u=22ms^{-1} at the tropopause located at approximately 8.5km, giving a shear of Λ=2.5$\times$10^{-3}s^{-1}. In the troposphere a constant buoyancy frequency of N=10^{-2}s^{-1} was used, the stratospheric buoyancy frequency was $4N$, and typical mid-latitude values of the Coriolis parameter f and planetary PV gradient β were used. The initial PV field was an upstream tilted PV wave within the troposphere (Figure 2(b)). Note that the TESV had little PV amplitude at the tropopause or ground at initial time (Figure 1(b)). The initial tilt was adjusted so that the evolved PV field resembled the evolved TESV structure in Figure 1.

Figure 2 shows the initial perturbation from the linear model, and the evolved perturbation at a time corresponding to 24 hours, in terms of PV and v. The evolved PV field (Figure 2) shows that the initially tilted PV has untilted, and excited CRWs at the tropopause and ground. In Figure 2 the tropopause is located at Z=0.7 where Z has been nondimensionalised by a height scale $H = (f/N)^2\Lambda/\beta \approx$15km. The maximum amplitude of the perturbation is at the tropopause; the interior PV has a smaller amplitude and there is an against-shear tilt that is also seen for the evolved TESV (Figure 1(d)). This shows that PV unshielding (the Orr mechanism) is not the only growth mechanism for the TESV perturbations, but that growth by resonant excitation of the CRWs (abbreviated to 'resonance') also occurs. The perturbation shown in Figure 2 resembles the SV at initial and final time. Therefore, we argue that the evolution of the SV is well described by the same three components and the same

DOI: 10.1002/qj

growth mechanisms. The PV anomalies at tropopause level and potential temperature anomalies at the ground are excited with similar phases relative to the interior PV structure as in the simple model with steady shear flow.

2.3 Pseudo Targeted Observation Profiles

A perturbed analysis was constructed by adding wind and temperature perturbations from the TESV onto a 1200 UTC analysis for the same day (the 1200 UTC CONTROL analysis detailed in IRV09 that was constructed from a hindcast run assimilating only routine observations during the period of the GFDex field campaign). Sets of pseudo targeted observations containing a singular vector structure 'SSV', were then created by taking profiles of u, v and temperature (T) through the perturbed analysis. A control set of pseudo targeted observations 'NOSV' was also created whereby profiles of u, v and T were taken from the unperturbed analysis. This control set of pseudo observations was required because the TESV perturbations were added to an analysis and not the background field (the background field is valid at 0900 UTC and the TESV perturbations at 1200 UTC). The addition of the TESV perturbations to the analysis (rather than directly to the background field) has the effect of adding noise to the observations, i.e. this removes the assumption of a perfect observation, as the observation minus background is not equal to the SV. The SSV and NOSV pseudo observations consisted of profiles of u, v and T, from 1000hPa to 200hPa with data every 50hPa. Where profiles intersected Greenland the nearest pressure level above the surface was used as the lowest data point, e.g. 650hPa over the Greenland plateau. Note that unlike real radiosonde or dropsonde observations, the pseudo targeted observations do not contain a humidity variable. This is to ensure that the model relative humidity field is not perturbed by either the SSV or NOSV pseudo observations because a dry TESV was used as the baroclinic structure.

The TESV perturbations were multiplied by a factor of 50 before being added to the analysis. The magnitude of the resulting perturbations at the latitude where the TESV has maximum amplitude is shown in Figure 3. The average perturbation size in v is 1.5ms^{-1} with a minimum of 0 and a maximum of 3.5ms^{-1}. The average observation minus background difference in v for the four GFDex experiments is between 2 and 5ms^{-1} (IRV09) which is slightly larger than the average SV perturbations used in this experiment. The observation minus background difference in T for the GFDex experiments is slightly smaller than the average SV perturbations shown in Figure 3(b). The size of the perturbations chosen here resulted in up to 1% of the total temperature observations processed being rejected; no wind observations were rejected. Using a smaller multiplication factor of 30 resulted in smaller perturbations, the same percentage of which were rejected during the observation processing. Using a larger multiplication factor of 100 resulted in unrealistically large perturbations for the type of meteorological situation, and caused the SSV profiles to become statically unstable. Therefore a multiplication factor of 50 is the largest possible for this experiment.

2.4 Experimental Setup

The hindcast runs used the Met Office incremental 4D-Var data assimilation scheme (Rawlins *et al.*, 2007) with a grid-spacing of 48km for the inner-loop and a six-hour window for observations, centred on the analysis time (1200 UTC). The operational observation and background errors were used; the background errors used at the beginning of the assimilation window are climatological and were calculated using forecast differences via the NMC

DOI: 10.1002/qj

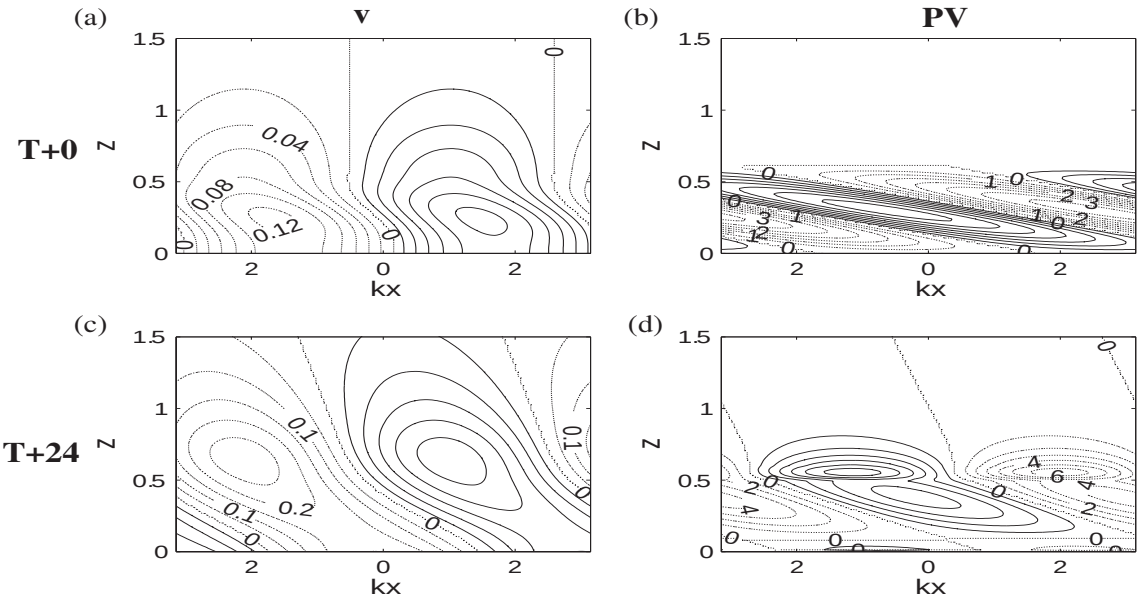

Figure 2. Cross-section through idealised model simulation illustrating the initial (a) v and (b) PV wave and the evolved (c) v and (d) PV. Height Z is non-dimensionalised; the tropopause is located at Z=0.7.

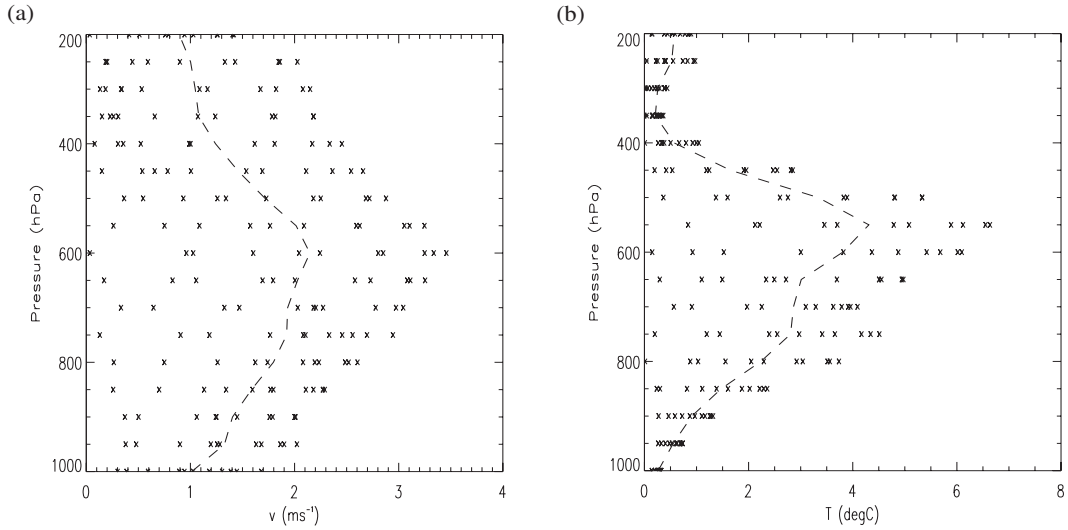

Figure 3. The magnitude of the TESV perturbations for 11 profiles along 66°N latitude. The size of each individual perturbation (crosses) and the level-average perturbation (dashed line) for (a) v and (b) T.

method (Parrish and Derber, 1992) with some modifications (Ingleby, 2001). They are represented via a transform to control variables, and implicitly evolved during the six-hour assimilation window. The forecast model was the Met Office Unified Model (MetUM), version 6.1. The model is non-hydrostatic and fully compressible, with a semi-implicit, semi-Lagrangian numerical scheme and uses the new dynamics formulation as its dynamical core (see Davies *et al.* (2005) for a detailed description). The model was run over a limited-area domain covering the North Atlantic and Europe (the operational North Atlantic European domain) on a rotated grid with a horizontal grid spacing of 24km and 38 vertical levels. Lateral boundary conditions were provided by the global control forecast of the Met Office Global and Regional Ensemble Prediction System (MOGREPS).

The pseudo targeted observations were arranged in a grid in order that the singular vector structure could be

DOI: 10.1002/qj

Table I. Experiment Details

Experiment	Number of sondes	Latitudinal spacing (degrees)	Longitudinal spacing (degrees)	Observation Errors (×operational)
N55_grid	55	2	2.5	1
N55_halfcov	55	2	2.5	0.5
N30_grid	30	2	5	1
N08_grid	8	4	10	1
N08_nogrid	8	3	5	1

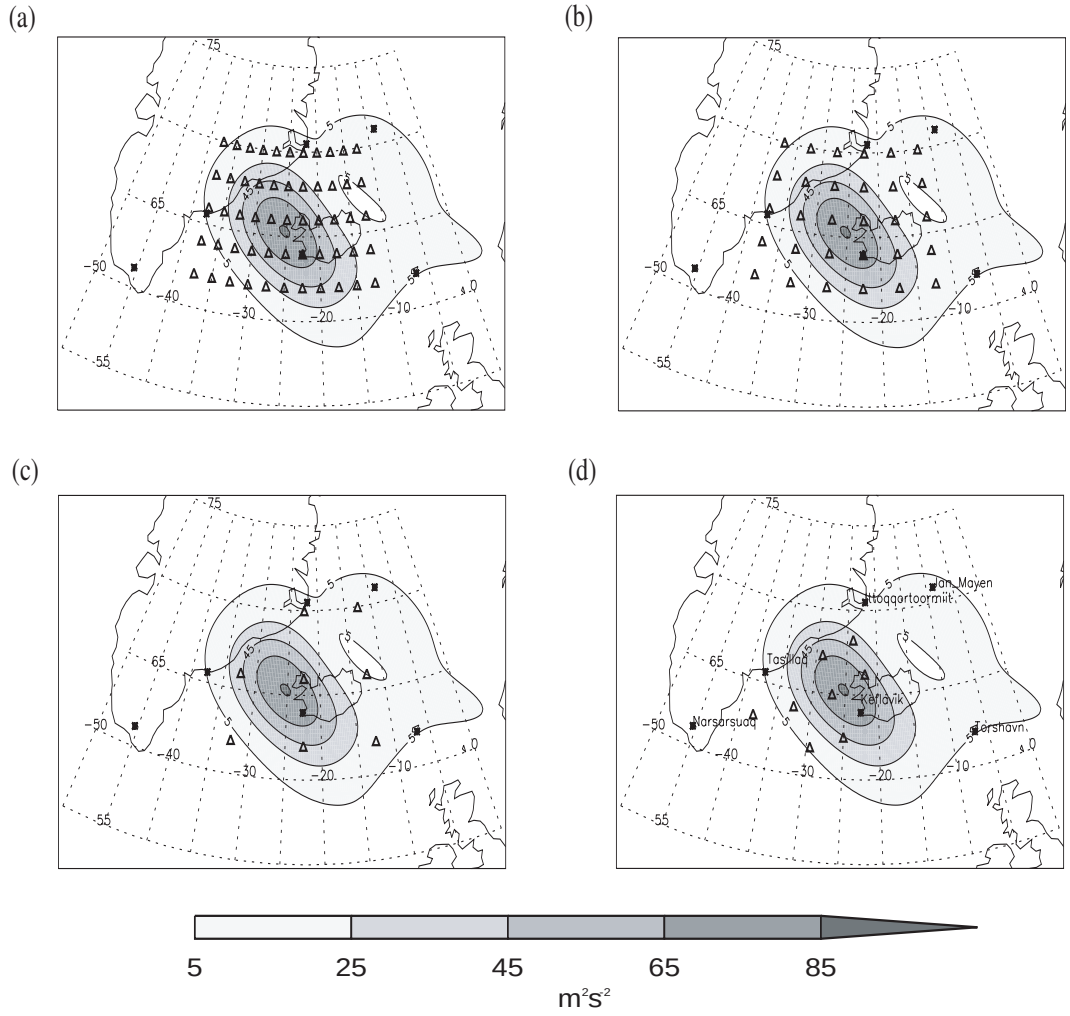

Figure 4. The locations of the pseudo targeted observations (triangles) for the experiments: (a) N55_grid, (b) N30_grid, (c) N08_grid and (d) N08_nogrid - 8 sondes along the flight track from the 01 March targeting case. The locations of nearby radiosonde stations are marked with asterisks, and are labelled in (d). The total energy of 50 times the initial SV perturbations summed over the 850, 500 and 250 hPa levels (contours) marks the location of the TESV.

fully captured by the pseudo observations. Five pairs of hindcasts (each pair comprising a SSV and NOSV experiment) were run; the details of the experiments are given in Table I. The locations of the pseudo targeted observations relative to the TESV structure are shown in Figure 4, where the total energy of the TESV perturbations, TE, is given by:

$$TE = \frac{1}{2}(u^2 + v^2) + \frac{1}{2}\frac{c_p}{T_{ref}}(T^2), \qquad (1)$$

DOI: 10.1002/qj

where c_p is the specific heat capacity and T_{ref} is a reference temperature of 300K. Each hindcast took the background field and assimilated the set of pseudo observations (SSV or NOSV) for the 1200 UTC 01 March 2007 forecast to produce an analysis. The number of pseudo observation profiles was varied from a regular grid of 55 'N55_grid' (Figure 4(a)) to 30 'N30_grid' (Figure 4(b)) to 8 'N08_grid' (Figure 4(c)). The size of the grid of observations was designed to cover the TESV structure, with minimum spacing between the pseudo observations on the order of the horizontal correlation length scales used in the assimilation. This is approximately 2° latitude and 2.5° longitude at 66°N, therefore the maximum number of sondes used in the experiments was 55. A further experiment was run with 8 pseudo observation profiles located along the 01 March flight track, at the same points as the targeted dropsondes, 'N08_nogrid' (Figure 4(d)). To test the influence of the weighting given to the observations during the assimilation process an additional experiment assimilated the 55 pseudo observation profiles on a grid, but reduced the observation errors (specified as standard deviations) for the pseudo observations only to half the operational values: 'N55_halfcov'. This increased the relative weighting of the pseudo observations.

The pseudo targeted observations were treated as radiosonde observations in the observation processing and assimilation (and the operational radiosonde observation errors were used). The hindcasts assimilated all available routine observations (e.g. the regular radiosonde, station, satellite and aircraft data) in addition to the pseudo targeted observations, with the exception of radiosonde soundings from Keflavik, Tasiilaq and Ittoqqortoormiit (Figure 4(d)). These data were denied from the assimilation as they were located within a radius of 150km of a pseudo targeted observation. This radius was used as the observation processing system compares the observation-background departure of two like observations located within 150km of each other. Removing these radiosonde observations avoided having two different profile observations in approximately the same location, that contained differing information.

The maximum area covered by pseudo targeted observations is approximately 1x10^{6}km^2, i.e. ten times larger than the area covered by dropsonde observations during GFDex, and the maximum number of observations is 55. Leutbecher *et al.* (2002) showed that to significantly impact the forecast, 10-40 targeted observations covering an area of 3x10^{6}km^2 were required. The N30_grid and N55_grid experiments should therefore include sufficient observations to impact the forecast, although the area covered by these experiments is three times smaller than in Leutbecher *et al.* (2002). As the number of pseudo observations decreases in the experiments, the longitudinal spacing is increased and so the resolution of the SV structure is decreased. Therefore in theory the N55_grid experiment should best capture the SV as this experiment has the highest resolution of data available to the data assimilation scheme.

Example SSV and NOSV profiles from the N55_grid experiment are compared in Figure 5. The addition of the 50 times SV perturbation results in changes in the profiles assimilated. There are minor changes to the strength of the low-level jet seen in the v profile with the addition of the perturbations generally resulting in a weakening of the low-level southerly winds; Figure 5(b) shows a weakening of 2ms^{-1} at 800hPa. The perturbation to the potential temperature field results in a reduced lapse rate below 700hPa (Figure 5(c)), with a weak inversion added in the more easterly profiles (not shown). The zonal wind (Figure 5(a)) exhibits a strong positive shear with

DOI: 10.1002/qj

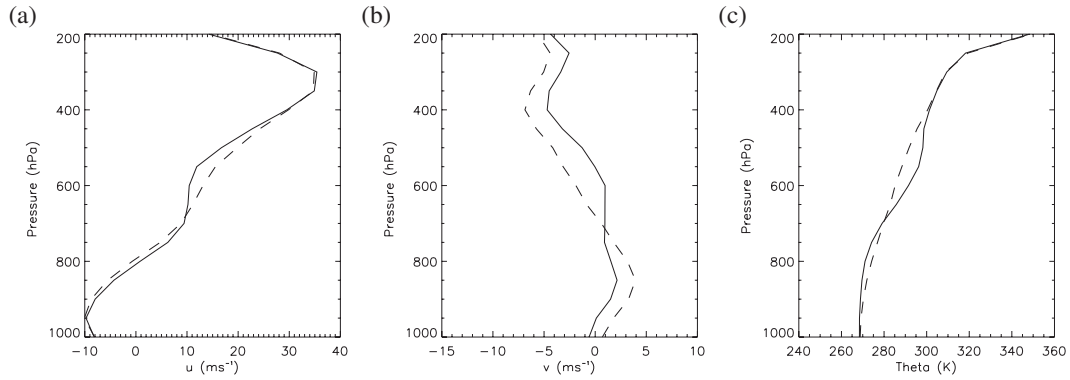

Figure 5. Pseudo observation profiles from the N55_grid experiment at 66°N 25°W for the SSV (solid lines) and NOSV (dashed lines) profiles for three variables: (a) u, (b) v and (c) potential temperature (theta).

height up to the tropopause; the perturbations introduce a midlevel weak shear layer.

3 Structure of Analysis Increments

To assess the ability of the data assimilation scheme to produce a tilted increment that captures the SV structure, the vertical structure of the difference of the SSV analysis increment and NOSV analysis increment was compared to that of the SV. As the analysis increments do not contain PV as a variable, the Ertel PV, q, of the analysis increments was calculated from the u, v and potential temperature, θ, fields:

$$q = -g\left\{-\frac{\partial v}{\partial p}\frac{\partial \theta}{\partial x} + \frac{\partial u}{\partial p}\frac{\partial \theta}{\partial y} + \left(\frac{\partial v}{\partial x} - \frac{\partial u}{\partial y} + f\right)\frac{\partial \theta}{\partial p}\right\}, \tag{2}$$

using isobaric co-ordinates and neglecting horizontal gradients in the vertical wind component. Figure 6 shows the difference of the SSV analysis increment and NOSV analysis increment for the different experiments compared to the SV perturbations. Note Figure 6(a) and (b) is equivalent to Figure 1(a) and (b), plotted on a different scale. First considering the N55_grid experiment only (Figure 6(c) and (d)), the analysis increment difference clearly captures the SV structure, showing a structure that is tilted against the shear, with a maximum in the mid-troposphere that is in phase with that of the SV. The maximum of the difference of the SSV and NOSV analysis increment in v is larger than for the SV and comparable for the PV field. The difference of the SSV and NOSV analysis increment can be larger than the SV because the observation minus background field is not equal to the SV because the pseudo-observations are generated by the addition of the SV to an analysis field, not a background field. A noticeable difference is that the tilt (from the vertical) of the difference of the SSV analysis increment and NOSV analysis increment is increased compared to the SV. The weaker variation in the horizontal is likely to result from the barotropic nature of the structure functions used in the assimilation process which control the spreading of data; this could be quantitatively assessed by analysing the analysis increment resulting from the assimilation of a single observation. The lack of tilt in the structure functions would result in a reduction of horizontal gradients and an increase of the tilt of the strongly tilted singular-vector perturbation that was present in the observations.

With a decreasing number of pseudo observations assimilated (Figure 6(e)-(l)), the SV structure becomes less well-represented. The SV is captured to some extent by all experiments, with the v and PV perturbations exhibiting a tilt against the wind shear which is flatter than for the SV. The amplitude of the difference of the SSV and NOSV analysis increment decreases as the

DOI: 10.1002/qj

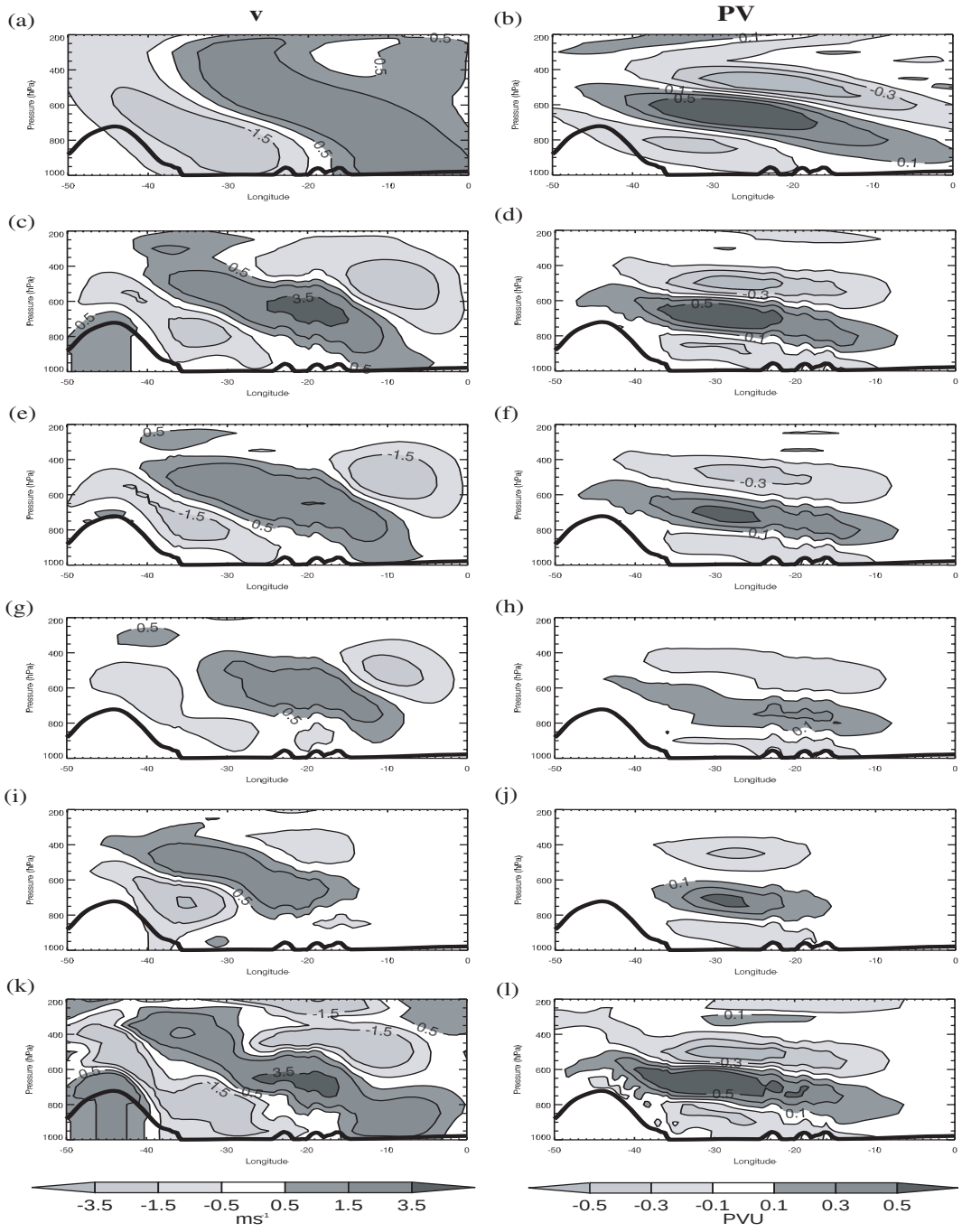

Figure 6. Cross-sections along 66°N from 50°W to 0°W showing v (left column) and PV (right column) for (a) and (b) the SV perturbation. (c) - (l) show the SSV-NOSV analysis increment for the (c) and (d) N55_grid, (e) and (f) N30_grid, (g) and (h) N08_grid, (i) and (j) N08_nogrid and (k) and (l) N55_halfcov experiments. The surface pressure (thick black line) is used to show the orography.

number of pseudo sondes assimilated in a regular grid decreases. When only 8 sondes are assimilated along the flight track the perturbation becomes more confined as the area covered by the sondes is decreased and the phase of the perturbation is shifted upstream (Figure 6(j)). When the N55_grid experiment is repeated with the observation errors halved (N55_halfcov) the increased weighting given to the observations during assimilation causes the amplitude of the SSV-NOSV analysis increment difference to be larger than that of the SV and spurious structures appear, particularly in v (Figure 6(k) and (l)) near the slope of Greenland.

DOI: 10.1002/qj

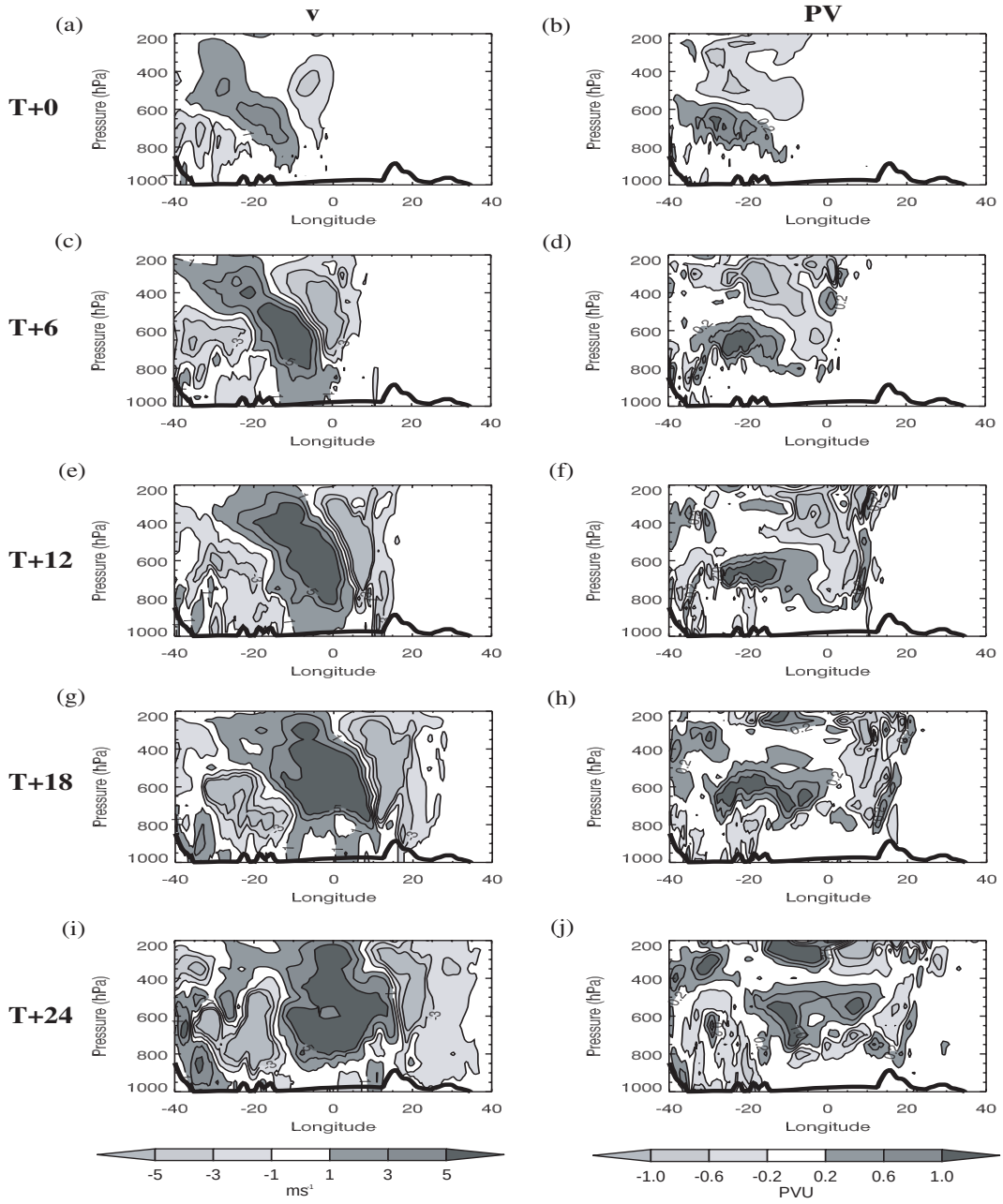

Figure 7. Cross-sections at 66°N from 40°W to 40°E showing the SSV-NOSV forecast difference for v (left column) and PV (right column) for the N55_grid experiment for forecast times of (a) and (b) 0 hours, (c) and (d) 6 hours, (e) and (f) 12 hours, (g) and (h) 18 hours and (i) and (j) 24 hours. The orography is represented using the surface pressure (thick black line).

4 Forecast Evolution

The evolution of the tilted structure in the analysis increments is seen by running 24-hour forecasts with the full nonlinear MetUM, and examining the SSV-NOSV forecast differences. In comparing the structure of these with the structure of the SV it is important to remember that the SV calculation is at T42 resolution (approximately 300km) and the nonlinear forecasts are run on a 24km grid, therefore the SSV-NOSV perturbations will contain finer-scale structure than the SV. The v and PV SSV-NOSV forecast differences are shown in Figure 7 for the N55_grid experiment. Note that the cross-section plotted has been expanded from the cross-sections plotted in Figure 6 (and match that plotted in Figure 1) so that the downstream development of the perturbations can be seen. The SSV-NOSV perturbation is initially tilted, and untilts

DOI: 10.1002/qj

as it evolves during the forecast. This untilting can be seen in both the v and PV components but is clearest in the v component; the PV component is noisier due to the advection of finescale PV anomalies in three dimensions (the perturbation is not planar as in the idealised experiments). The growth of the SSV-NOSV perturbation is consistent with growth through PV-unshielding (Hoskins *et al.*, 2000) and resonance, as in the SV and idealised model (Figure 2). The perturbation becomes less confined as it moves downstream, untilts, and moves up towards the tropopause. The evolved v field shows a dipole in the v perturbation, which has significant amplitude from 200-800 hPa and untilts with time (Figure 7(i)). There is also a horizontal dipole in the evolved PV perturbation at 200hPa (Figure 7(j)), and a positive perturbation below it. The positive part of the dipole structure is greater in amplitude than for the evolved SV perturbation (Figure 1(d)). The evolved forecast perturbation for the N55 experiment is slightly out of phase with the evolved SV perturbation; the downstream propagation of the SSV-NOSV forecast perturbation is faster than for the SV (following the leading negative PV anomaly at 500hPa). The upper-level jet at 300hPa, visible in the u-wind field (Figure 5(a)), determines the speed with which the SV-like perturbations propagate downstream. The PV-unshielding and downstream development of the SSV-NOSV forecast seen in Figure 7 for the N55_grid experiment is seen for all experiments (not shown).

The perturbation (SSV-NOSV) forecasts at T+24 (Figure 7(j)) have features in common (mainly east of 10W) with the SV structure (Figure 1(d)) and the PV distribution in the simple model (Figure 2(d)). Although the perturbation forecast is obtained by differencing two nonlinear simulations of the full NWP model, elements of the structure and their relative phase can be anticipated by breaking down the perturbation into three wave-like components following linear dynamics under the influence of uniform shear. In particular, the strong perturbations at the tropopause arise through excitation of the upper Rossby wave-like structure by the interior PV as it tilts over in the shear flow. However, there are exceptions, especially in the lower troposphere to the west of 10°W where the perturbation forecast contains large anomalies that are not explained by the SV or simple model.

The total energy contained in the initial and evolved SV and N55_grid SSV-NOSV forecast perturbations is shown in Figure 8, where the total energy has been calculated using (1) and summed over the 850, 500 and 250 hPa levels. Note that the total energy plotted in Figure 8(a) is equivalent to that in Figure 4, with the scale modified so that the total energy of the SSV-NOSV perturbations is clearer. The shape and area of the initial energy of the SSV-NOSV perturbations is a reasonable match to that of the SV perturbation, although the magnitude is reduced; this is also the case for the other experiments (not shown). The initial singular-vector like structure of the SSV-NOSV perturbations moves downstream to the same location as the SV perturbation. However, consistent with the amplitude of the initial energy, the amplitude of the evolved perturbation is also reduced compared to the SV perturbation and decreases for decreasing number of pseudo observations assimilated (not shown). This agrees with the conclusions from examining the difference of the SSV and NOSV analysis increments that the SV perturbation is better sampled with a greater number of sondes.

5 Perturbation Growth Rates

In order to compare the growth rate of the SSV-NOSV perturbations with that of the SV perturbations, the total energy plotted in Figure 8 is spatially integrated. As the

DOI: 10.1002/qj

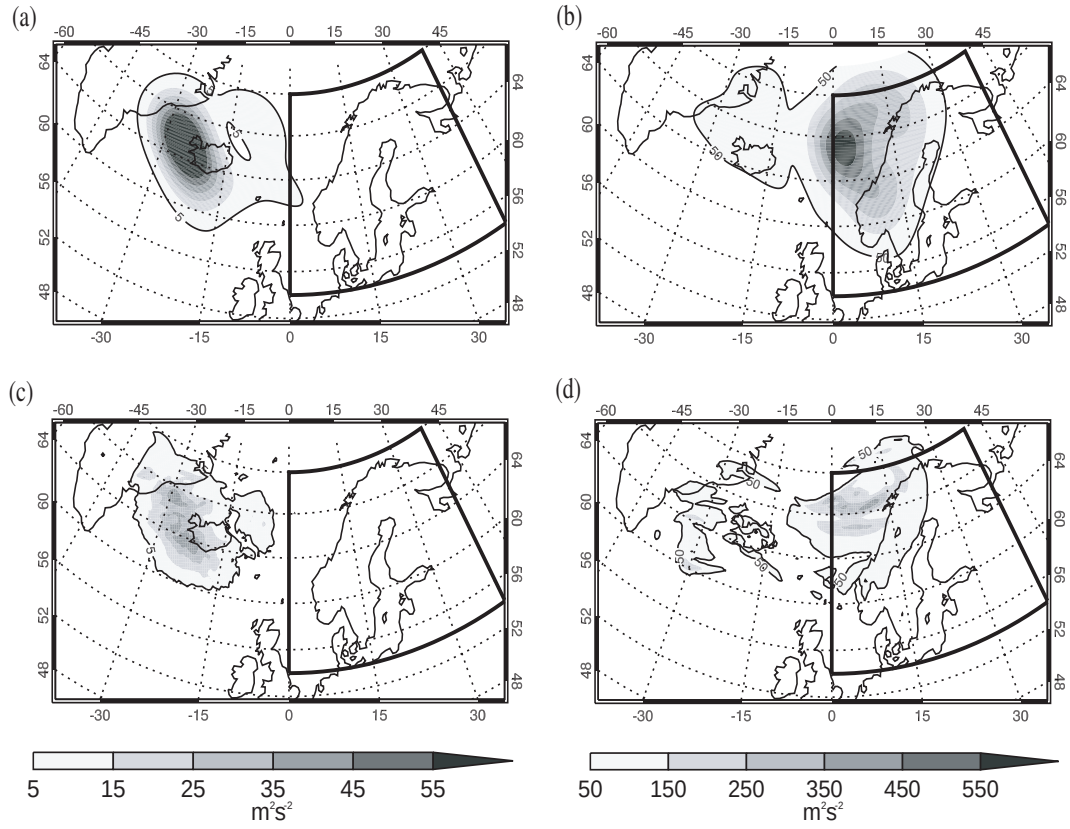

Figure 8. Vertically integrated total energy at initial time (left column), and after 24 hours evolution (right column) for (a), (b) TESV perturbations, and (c) and (d) the SSV-NOSV forecasts for the N55_grid experiment. The minimum contour is $5\mathrm{m}^2\mathrm{s}^{-2}$ (left column) and $50\mathrm{m}^2\mathrm{s}^{-2}$ (right column) and is marked by a thin black line. Note the factor of ten difference between the scales for the plots in the left and right columns. The Scandinavian verification region is marked by a thick black line.

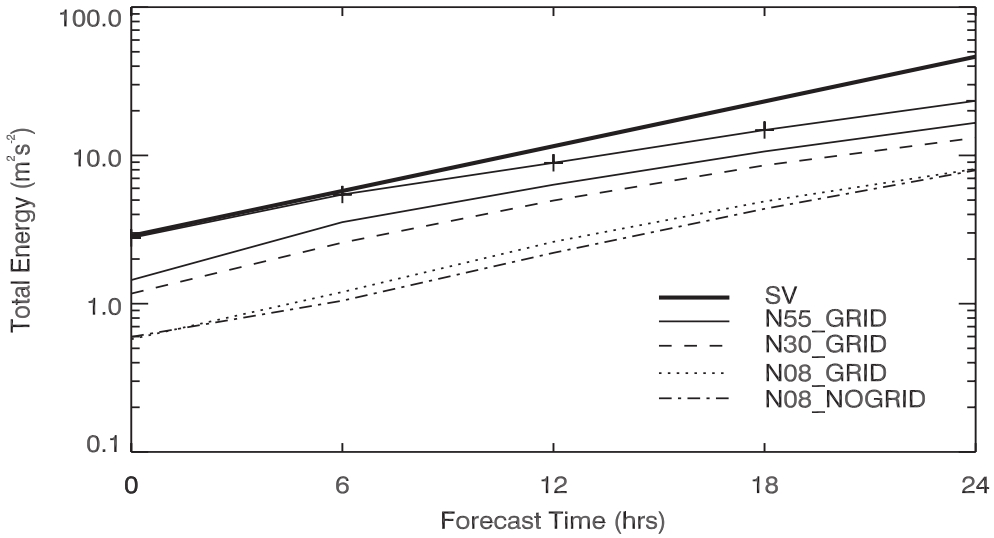

Figure 9. Spatially integrated total energy, normalised by the mass of the domain, for the SV perturbation (thick line) and SSV-NOSV forecasts: N55_grid (solid line), N30_grid (dashed line), N08_grid (dotted line), N08_nogrid (dashed-dotted line) and N55_halfcov (solid line with crosses through it). Values between 0 and 24 hours forecast time for the SV perturbations were obtained by assuming an exponential error growth between the two times. Note the log scale on the y-axis.

SV data is only available for the initial and final evolved state, exponential growth is assumed at intermediate times in order to compare the growth of the SSV-NOSV perturbations with that of the SV. Figure 9 shows the spatially

DOI: 10.1002/qj

integrated total energy of the SV perturbation and SSV-NOSV perturbations for all experiments, plotted with a log scale on the y-axis. The initial energy for the SSV-NOSV experiments is typically less than for the SV perturbation. This gap can be at least partly explained by the observation processing and data assimilation, as assimilating the 55 sondes with reduced observation error variances (i.e. giving them greater weighting) increases the initial energy and eliminates this gap although this perturbation appears to have a smaller growth rate. The gradient of the lines is similar for all experiments except the N55_halfcov experiment, meaning that the exponential growth rates are similar.

Table II shows the average exponential growth rate for all experiments and SV perturbations. The SV perturbation growth rate is 2.78day^{-1} which is higher than the maximum Eady growth rate for this region of 2.0day^{-1}, consistent with the results of Badger and Hoskins (2001) who showed that the initial growth rate of against-shear tilted perturbations was higher than that of the fastest growing normal mode. The SSV-NOSV perturbations exhibit growth rates that are up to 20% less than for the SV but larger than the Eady growth rate. The inner product of the SV and SSV-NOSV perturbations was also calculated for all cases, using the total energy norm (1), after normalising the perturbations. The inner products (projection coefficients) are given in Table II. The higher the projection coefficient, the more similar the SV and SSV-NOSV perturbation (the projection coefficient would be 1 if the perturbations were the same). The N55_grid experiment has the highest projection coefficient of 0.72, and the value of the projection coefficient decreases as the SV is represented with fewer sondes. The N55_halfcov experiment has the smallest projection onto the SV, with a projection coefficient of only 0.52. This explains the small growth rate seen for this experiment. As the initial energy contained within the N55_halfcov experiment is high, this suggests that much of the initial energy is from spurious structures that decay during the forecast. Therefore despite the initial perturbations not fully capturing the SV structure, the growth of the perturbations does closely resemble that of a SV-like perturbation.

Table II. Perturbation growth rates and projection onto SV structure, defined using a total energy inner product

Experiment	Average Growth Rate (day^{-1})	Projection Co-efficient
SV	2.78	1.0
n55_grid	2.44	0.72
n30_grid	2.42	0.71
n08_grid	2.65	0.64
n08_nogrid	2.59	0.62
n55_halfcov	2.13	0.52

6 Conclusions

This paper examines the ability of the data assimilation scheme to extract important dynamical information, such as upshear tilt, from targeted observations and use it to correct an initial condition error of a baroclinic structure. Sets of targeted pseudo observations were assimilated which contained such a tilted structure that was neither present in the background field nor the routine observations. The structure was obtained by calculating the leading total energy singular vector for the 01 March 2007 GFDex targeting case detailed in Irvine *et al.* (2009).

The results presented clearly show that a 4D-Var scheme with 6-hour data assimilation window is capable of extracting baroclinic information from a grid of observations. The extent to which the data assimilation scheme was able to reproduce the SV structure that was present in the observations is dependent on how well the SV structure is captured by the targeted observations that are assimilated, and the weighting given to the pseudo

DOI: 10.1002/qj

observations (the observation error variance) during the assimilation process.

The analysis increments show a baroclinic structure most closely representing the SV perturbations for a grid of 55 sondes (covering an area of approximately $1x10^6 km^2$). This experiment had the largest projection onto the SV, of 0.72. The structure of the SV is reproduced in the analysis increments even with a grid of 8 sondes, although the amplitude is reduced and tilt (from the vertical) is increased compared to the SV as the number and density of observations are decreased. The increased tilt can be explained by a smearing-out of the tilted structure in the horizontal by the background error covariance in the assimilation process. For 8 pseudo observations along a flight track, the SV structure was less well represented by the observations and the resulting analysis increments showed a weakly tilted structure of reduced magnitude that was phase-shifted upstream of the SV, particularly in v. Nevertheless the projection onto the SV was still 0.62. Whilst these experiments used idealised observations, and (aside from the N08_nogrid experiment) approximately matched the target area to the area of initial condition error, the results have implications for operational targeting experiments. For example the GFDex targeting experiments released 7-11 sondes, similar to the N08 experiment here, over an area similar to the N08_nogrid experiment. These results suggest that this level of sampling would have been insufficient to fully capture any tilted structures, and as a result it would have been difficult for the data assimilation scheme to produce a tilted increment. In operational targeting it is more difficult to a priori identify the region of initial condition error, and adequately sample it with the available resources. These results further support the results of Leutbecher *et al.* (2002) and Buizza *et al.* (2007) that sensitive areas must be sufficiently sampled for the targeted observations to have a significant forecast impact and that by only partially sampling the sensitive region the forecast impact can be reduced (Buizza and Montani, 1999).

The structure and growth of the forecast perturbations produced most closely resemble that of the SV for the experiment assimilating 55 sondes. When 30 sondes are assimilated the increased longitudinal spacing from 2.5 to 5 degrees compared to the 55 sonde experiment makes only a small difference; the assimilation scheme is still able to extract the baroclinic structure from the pseudo targeted observations. All experiments show an untilting of the initial tilted PV and v perturbations that is consistent with growth by 'PV-unshielding' (Hoskins *et al.*, 2000) and an excitation of counter-propagating Rossby waves at the ground and tropopause (De Vries *et al.*, 2009), that was shown by the simple model.

The initial energy contained in the forecast perturbations, as measured by total energy, is smaller than for the SV perturbation in all experiments when using the operational observation error variances. The initial energy is decreased as the number of sondes assimilated is decreased. This gap in initial energy occurs because the data assimilation scheme does not adjust the background fully towards the observations, as it takes account of the errors in the observations. When the weighting given to the observations is increased by halving the pseudo observation errors this initial energy gap becomes close to zero. However, part of this initial energy comes from spurious structures in the initial forecast field, and the projection of the perturbation onto the SV is small, at only 0.52. As a result the average growth rate is smallest for this experiment.

The results from this study are in contrast to Rabier and Courtier (1992), Johnson *et al.* (2006) and Thépaut

DOI: 10.1002/qj

et al. (1996) who found that an assimilation window of 12-24 hours was required to correct a growing error and produce an analysis increment of a baroclinic structure (although Thépaut *et al.* (1996) assimilated only single observations, so their results may not be strictly comparable to this study). The pseudo targeted observations used in this experiment were placed only three hours into a six-hour data assimilation window, when the background errors are likely to be little different from climatology. However it was seen that with only a few observations capturing the SV structure the 4D-Var system could not correct as much of the growing error. It is likely that an improved 4D-Var or hybrid data assimilation system that uses properly flow dependent background errors would be able to correct more of the growing error with fewer observations.

It is important to note that the results in this paper were obtained using a single TESV to approximate a baroclinic structure; the use of a different SV has not been tested and would not necessarily yield the same results. The use of a longer optimisation time SV would change the structure of the assumed baroclinic structure, as longer optimisation time TESVs exhibit a stronger tilt against the vertical wind shear and are more confined in the vertical. The choice of initial norm also affects the structure of SVs, however Lawrence *et al.* (2009) found that TESVs have a similar vertical structure to SVs computed with an initial metric based on the analysis error covariance (for example Hessian SVs); therefore the use of Hessian SVs should yield similar results.

Acknowledgements

Andrew Lawrence at ECMWF provided the TESV sensitive area predictions. We acknowledge Brian Hoskins and Ian Renfrew for helpful discussions during the project. We acknowledge Richard Swinbank, Richard Dumelow and Richard Marriott at the Met Office for providing access to Met Office machines and technical support. We also acknowledge technical support from the National Centre for Atmospheric Science Computational Modelling Support team. The code for the Rossby wave model was kindly provided by Hylke De Vries. The study was supported by a Natural Environment Research Council (NERC) grant (NE/C003365/1).

References

Badger J, Hoskins BJ. 2001. Simple initial value problems and mechanisms for baroclinic growth. *J. Atmos. Sci.* **58**: 38–49.

Buizza R, Cardinali C, Kelly G, Thepaut J. 2007. The value of targeted observations - Part II: the value of observations taken in singular vectors-based target areas. *Q. J. R. Meteorol. Soc.* **133**: 1817–1832.

Buizza R, Montani A. 1999. Targeting observations using singular vectors. *J. Atmos. Sci.* **56**: 2965–2985.

Buizza R, Palmer TN. 1995. The singular-vector structure of the atmospheric global circulation. *J. Atmos. Sci.* **52**: 1434–1456.

Coutinho MM, Hoskins BJ, Buizza R. 2004. The influence of physical processes on extratropical singular vectors. *J. Atmos. Sci.* **61**: 195–209.

Davies T, Cullen MJP, Malcolm AJ, Mawson MH, Staniforth A. 2005. A new dynamical core for the Met Office's global and regional modelling of the atmosphere. *Q. J. R. Meteorol. Soc.* **131**: 1759–1782.

De Vries H, Methven J, Frame THA, Hoskins BJ. 2009. An interpretation of baroclinic initial value problems: results for simple basic states with nonzero interior PV gradients. *J. Atmos. Sci.* **66**: 864–882.

Fourrié N, Marchal D, Rabier F, Chapnik B, Desroziers G. 2006. Impact study of the 2003 North Atlantic THORPEX Regional Campaign. *Q. J. R. Meteorol. Soc.* **132**: 275–295.

Hartmann DL, Buizza R, Palmer TN. 1995. Singular vectors: the effect of spatial scale on linear growth of disturbances. *J. Atmos. Sci.* **52**: 3885–3894.

Hoskins BJ, Buizza R, Badger J. 2000. The nature of singular vector growth and structure. *Q. J. R. Meteorol. Soc.* **126**: 1565–1580.

Hoskins BJ, Valdes PJ. 1990. On the existence of storm-tracks. *J. Atmos. Sci.* **47**: 1854–1864.

Ingleby NB. 2001. The statistical structure of forecast errors and its representation in the Met. Office Global 3-D variational data assimilation scheme. *Q. J. R. Meteorol. Soc.* **127**: 209–231.

DOI: 10.1002/qj

Irvine EA, Gray SL, Methven J, Renfrew IA, Bovis K, Swinbank R. 2009. The impact of targeted observations made during the Greenland Flow Distortion Experiment. *Q. J. R. Meteorol. Soc.* **135**: 2012–2029.

Johnson C, Hoskins B, Nichols N, Ballard S. 2006. A singular vector perspective of 4DVAR: the spatial structure and evolution of baroclinic weather systems. *Mon. Wea. Rev.* **134**: 3436–3455.

Langland RH. 2005. Issues in targeted observing. *Q. J. R. Meteorol. Soc.* **131**: 3409–3425.

Lawrence AR, Leutbecher M, Palmer TN. 2009. The characteristics of hessian singular vectors using an advanced data assimilation scheme. *Q. J. R. Meteorol. Soc.* **135**: 1117–1132.

Leutbecher M, Barkmeijer J, Palmer TN, Thorpe AJ. 2002. Potential improvement to forecasts of two severe storms using targeted observations. *Q. J. R. Meteorol. Soc.* **128**: 1641–1670.

Montani A, Thorpe AJ, Buizza R, Unden P. 1999. Forecast skill of the ECMWF model using targeted observations during FASTEX. *Q. J. R. Meteorol. Soc.* **125**: 3219–3240.

Morss RE, Emanuel KA. 2002. Influence of added observations on analysis and forecast errors: Results from idealized systems. *Q. J. R. Meteorol. Soc.* **128**: 285–321.

Parrish DF, Derber JC. 1992. The National Meteorological Center's spectral statistical-interpolation analysis scheme. *Mon. Wea. Rev.* **120**: 1747–1763.

Petersen GN, Thorpe AJ. 2007. The impact on weather forecasts of targeted observations during A-TReC. *Q. J. R. Meteorol. Soc.* **133**: 417–431.

Rabier F, Courtier P. 1992. Four-dimensional assimilation in the presence of baroclinic instability. *Q. J. R. Meteorol. Soc.* **118**: 649–672.

Rawlins F, Ballard SP, Bovis KJ, Clayton AM, Li D, Inverarity GW, Lorenc AC, Payne TJ. 2007. The Met Office global four-dimensional variational data assimilation scheme. *Q. J. R. Meteorol. Soc.* **133**: 347–362.

Renfrew IA, Moore GWK, Kristjánsson JE, Ólafsson H, Gray SL, Petersen GN, Bovis K, Brown PRA, Føre I, Haine T, Hay C, Irvine EA, Lawrence A, Ohigashi T, Outten S, Pickart RS, Shapiro M, Sproson D, Swinbank R, Woolley A, Zhang S. 2008. The Greenland Flow Distortion Experiment. *Bull. Am. Met. Soc.* **89**: 1307–1324.

Szunyogh I, Toth Z, Emanuel KA, Bishop CH, Snyder C, Morss RE, Woolen J, Marchok T. 1999. Ensemble-based targeting experiments during FASTEX: The effect of dropsonde data from the Lear jet. *Q. J. R. Meteorol. Soc.* **125**: 3189–3217.

Szunyogh I, Toth Z, Morss RE, Majumdar SJ, Etherton BJ, Bishop CH. 2000. The effect of targeted dropsonde observations during the 1999 Winter Storm Reconnaissance Program. *Mon. Wea. Rev.* **128**: 3520–3537.

Szunyogh I, Toth Z, Zimin AV, Majumdar SJ, Persson A. 2002. Propagation of the effect of targeted observations: The 2000 Winter Storm Reconnaissance Program. *Mon. Wea. Rev.* **130**: 1144–1165.

Thépaut JN, Courtier P, Belaud G, Lemaître G. 1996. Dynamical structure functions in a four-dimensional variational data assimilation: a case study. *Q. J. R. Meteorol. Soc.* **122**: 535–561.

DOI: 10.1002/qj